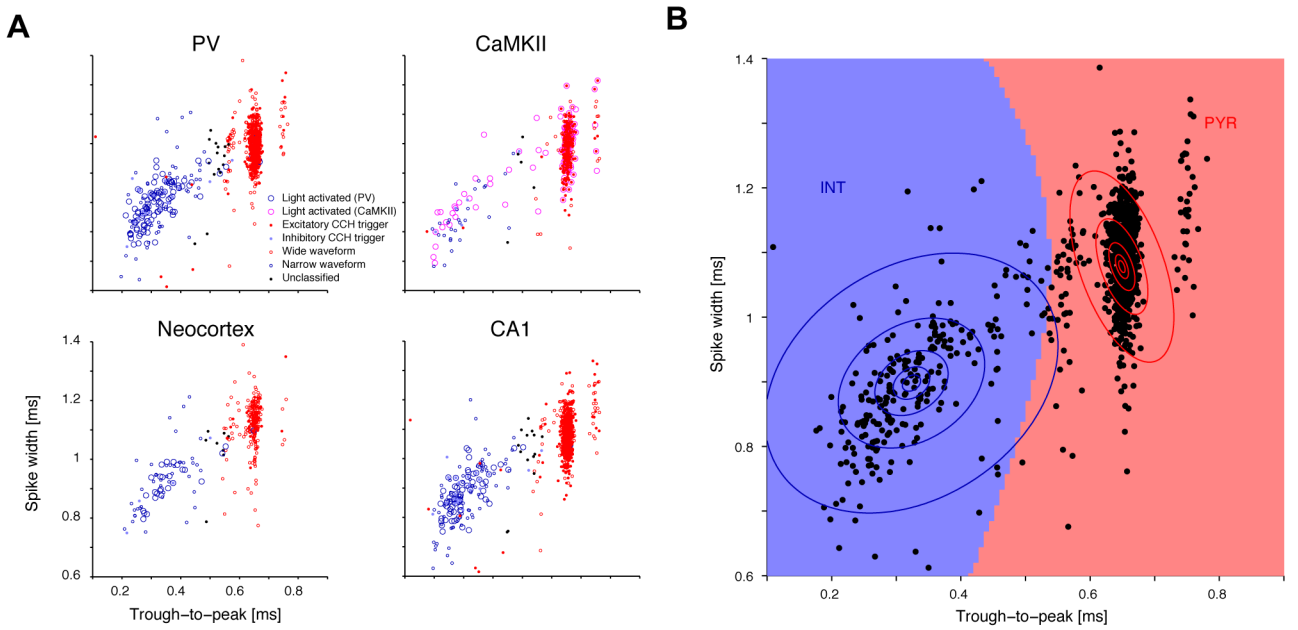

C

	CaMKII		PV		Total		All
	PYR	INT	PYR	INT (PV)	PYR	INT	
CX	82	21	162	54 (24)	244	72	316
CA1	227	35	680	133 (69)	907	168	1075
Total	309	56	842	184(93)	1151	240	1391

D

	CaMKII		PV		Total		All
	PYR	INT	PYR	INT (PV)	PYR	INT	
CX	54	17	138	30 (22)	192	47	239
CA1	203	29	204	56 (30)	407	85	492
Total	257	46	342	86 (52)	599	132	731

Figure S1. Cell type classification in freely-moving mice

(**A**) Unit tagging by optical activation and mono-synaptic connectivity. Top panels show data partitioned by the targeted cell type (PV, n=8 mice; CaMKII, n=4), whereas bottom panels partition the same data by the brain region. For presentation purposes, individual dots are jittered (SD, 6 μs). In all cases, the spike waveform features (trough-to-peak time and spike width) form two separable clusters, which correspond to the mono-synaptic and optical tagging. (**B**) Objective classification of units by waveform features. A 2-D Gaussian mixture model (GMM) was fit to the tagged units. Ellipses show iso-probability regions for each Gaussian, and background colors show the maximum a-posteriori (MAP) classification. Units close to the separatrix (p>0.05) were not classified; these units are shown as black dots in **A**. (**C**) Number of units used for cell type classification (**Figure 1, Figure S1**). CaMKII, animals expressing ChR2 in PYR cells (17 sessions in n=4 mice); PV, animals expressing ChR2 in PV interneurons (45 sessions in n=8 mice). 22 units for which classification confidence was low (p>0.05) are not included. PYR, pyramidal cells; INT (PV), putative inhibitory (light activated) interneurons. CX, somatosensory neocortex; CA1, CA1 pyramidal-cell layer. (**D**) Number of units used for wide-band analysis (all figures except **Figures 1, S1, and 7**). Only “optical” sessions are included (at least one unit was directly-activated during DC pulses, and the median DC gain for directly-activated units was at least 3). This yielded 16 sessions from 4 CaMKII mice and 22 sessions from 8 PV animals. An additional 175 PYR and 67 PV were recorded in CA1 of urethane-anesthetized PV mice (n=5 sessions from 5 animals); all acute sessions were optical and used for the results shown in **Figure 7**.

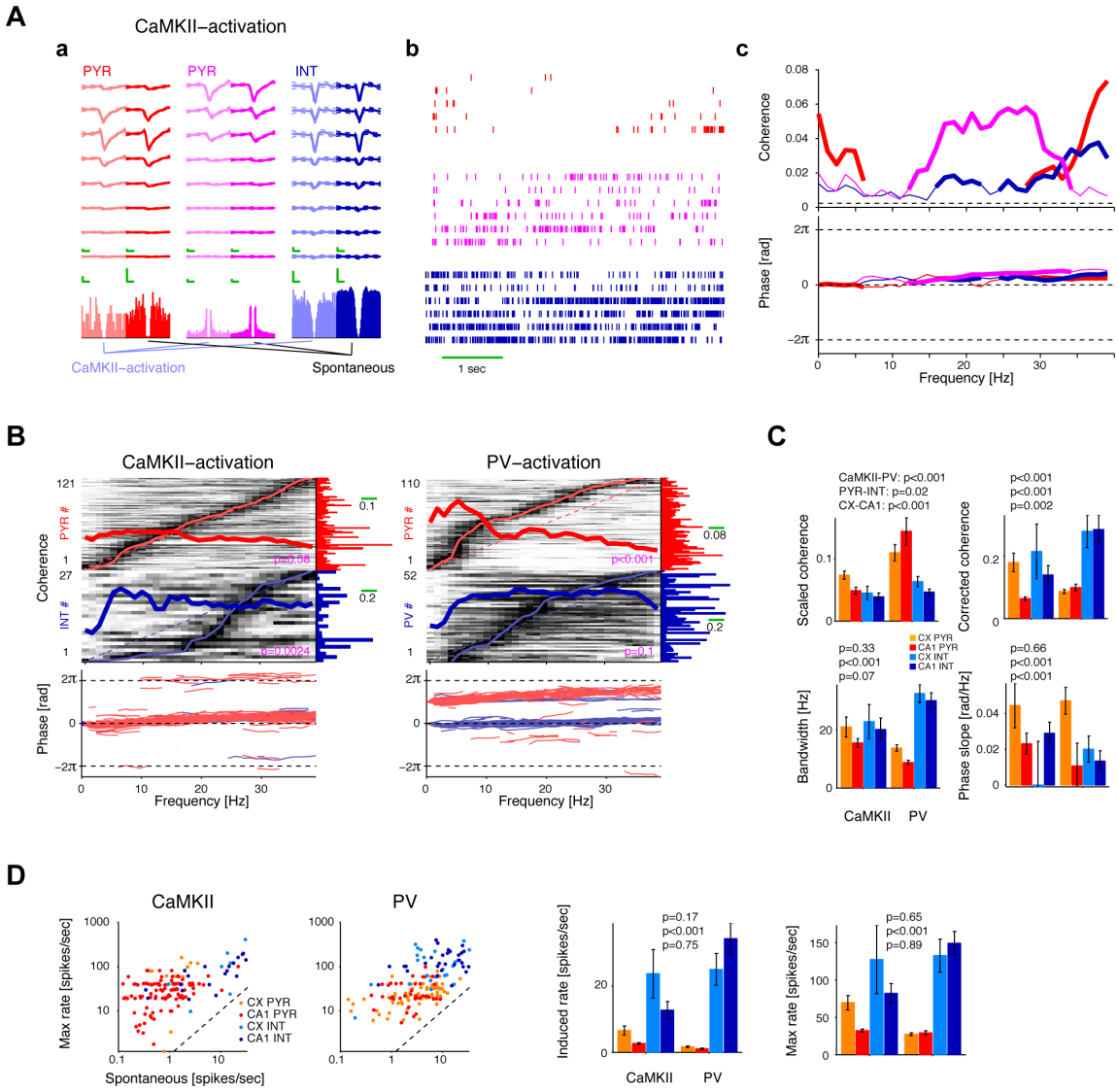

Figure S2. Band-limited spiking of pyramidal cells is centered at theta by inhibition

(**A**) Narrow-band PYR spiking during CaMKII activation. Example cluster of cells recorded in CA1 pyramidal layer during CaMKII activation. The three cells were recorded simultaneously from the same diode-probe shank. **a**, waveforms (mean and SD; calibration: 0.25 ms, 50 μV) and auto-correlation histograms (calibration: 10 ms, 10 spikes/sec). **b**, spiking activity (ticks) during chirp pattern application (6 consecutive trials; 405 nm light intensity, 1.25 mW/mm^2 at the shank center). **c**, Coherence and phase plots. Thick lines, frequency bands in which chirp-spiking coherence were significant. Dashed line shows mean chance coherence. Note that directly-activated PYR and indirectly-activated INT exhibit band-limited phase-locked spiking, and that the preferred chirp frequency differs for the two PYR cells. (**B**) Coherence and phase plots for the main datasets. Units are ordered by peak coherence frequency, phases are shown in a circular-linear plot, and other conventions are the same as in **Figure 2C**. During PV activation, PYR spike at chirp troughs and the distribution of peak frequencies differs from uniform (maximum in the theta band). (**C**) Statistics for frequency-domain analysis (complements **Figure 2D**). "Scaled" coherence is coherence divided by the square root of the mean firing rate over the entire chirp duration, and "corrected" coherence is coherence divided by the normalized input spectrum. Bandwidth is the longest stretch of significant coherence. P-values are for three 1-way Kruskal-Wallis tests; group means and SEM are shown. (**D**) Spiking rate during chirp-pattern activation. Induced rate: mean rate during the entire chirp. Spontaneous rate, baseline firing rate (no-light condition). Maximum rate, maximum over all bins in the spiking frequency-phase map. Maximum rate is higher for PV and may surpass 300 Hz during PV activation.

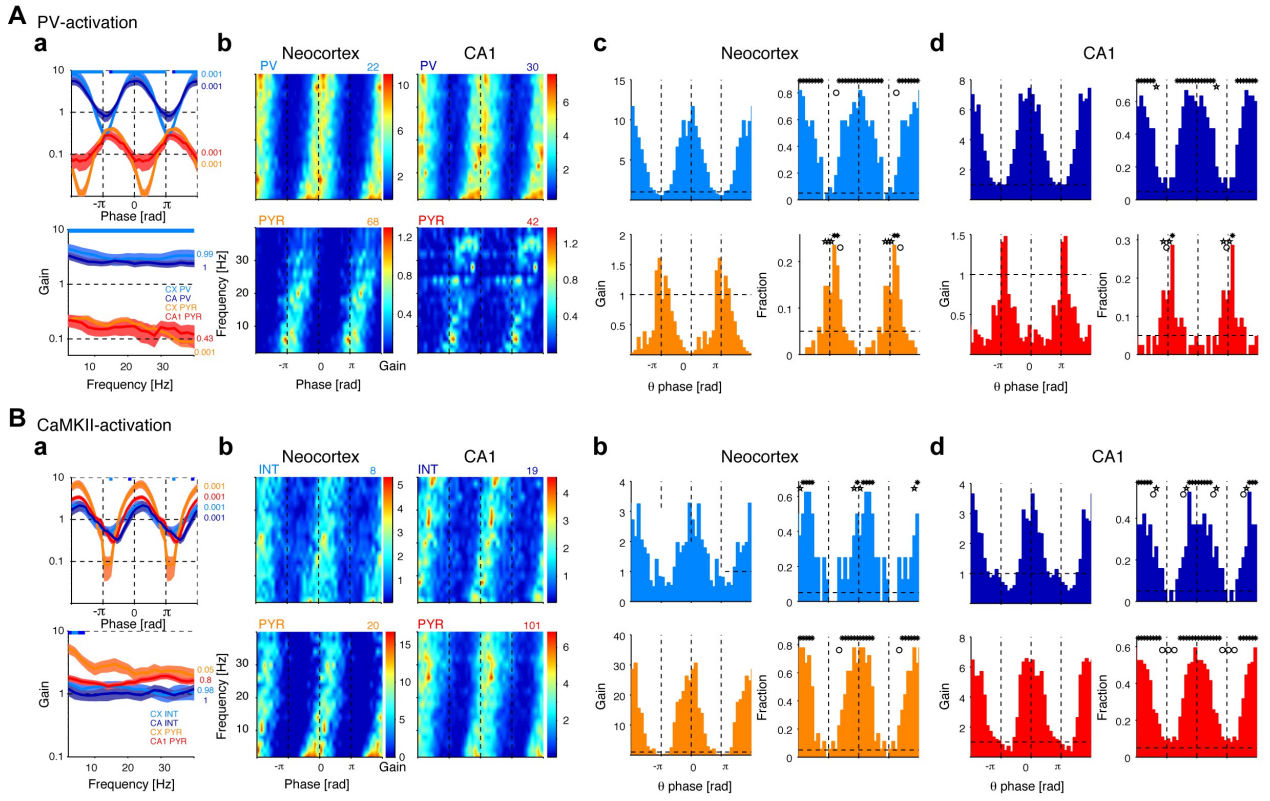

Figure S3. Pyramidal cells rebound at the trough of theta-band PV activation

(**A**) Frequency-dependent signaling induced by chirp-pattern PV photostimulation is similar in neocortex and CA1. **a**, Spiking gain marginals (mean±SEM), resolved by chirp phase (top) or frequency (bottom), are plotted by regions (light activated units only, same data as in **Figure 3Ab** but shown separately for CA1 and neocortex). Light/dark blue bars at top: p<0.01/0.005 (Bonferroni-corrected 1-way Kruskal-Wallis test comparing the 4 groups at each phase). P-values at right show results of intra-group Kruskal-Wallis tests comparing phases. PYR spiking is least suppressed during troughs of chirp-pattern PV activation **b**, Spiking gain maps (group means), plotted by chirp phase and frequency. PV tend to spike mainly during chirp peaks while PYR tend to spike mainly during the chirp troughs, predominantly at theta frequency. **c**, Detailed analysis for neocortical PV (top) and PYR (bottom) at the theta (4-11 Hz) band. Left, theta-band gain (averaged over all light-modulated units; horizontal dashed line shows gain=1); right, fraction of units with increased spiking in each theta-band chirp phase (gain>1; Bonferroni-corrected permutation test, p<0.05; horizontal dashed line). Symbols (circle/star/asterisk) above bars indicate phase bins for which the fraction of units exceeds chance level (5%) with p<0.05/0.01/0.001 (exact Binomial test). **d**, Same as **c**, for units recorded in CA1 during PV chirp-pattern application. (**B**) Same as **A**, during chirp-pattern CaMKII activation. Note that during theta-band CaMKII activation, both PYR and INT spike mainly around the chirp peaks, in both neocortex and CA1 region. In contrast, during theta-band PV activation, PV spike predominantly at the chirp peaks whereas PYR spike at (or just after) the chirp troughs.

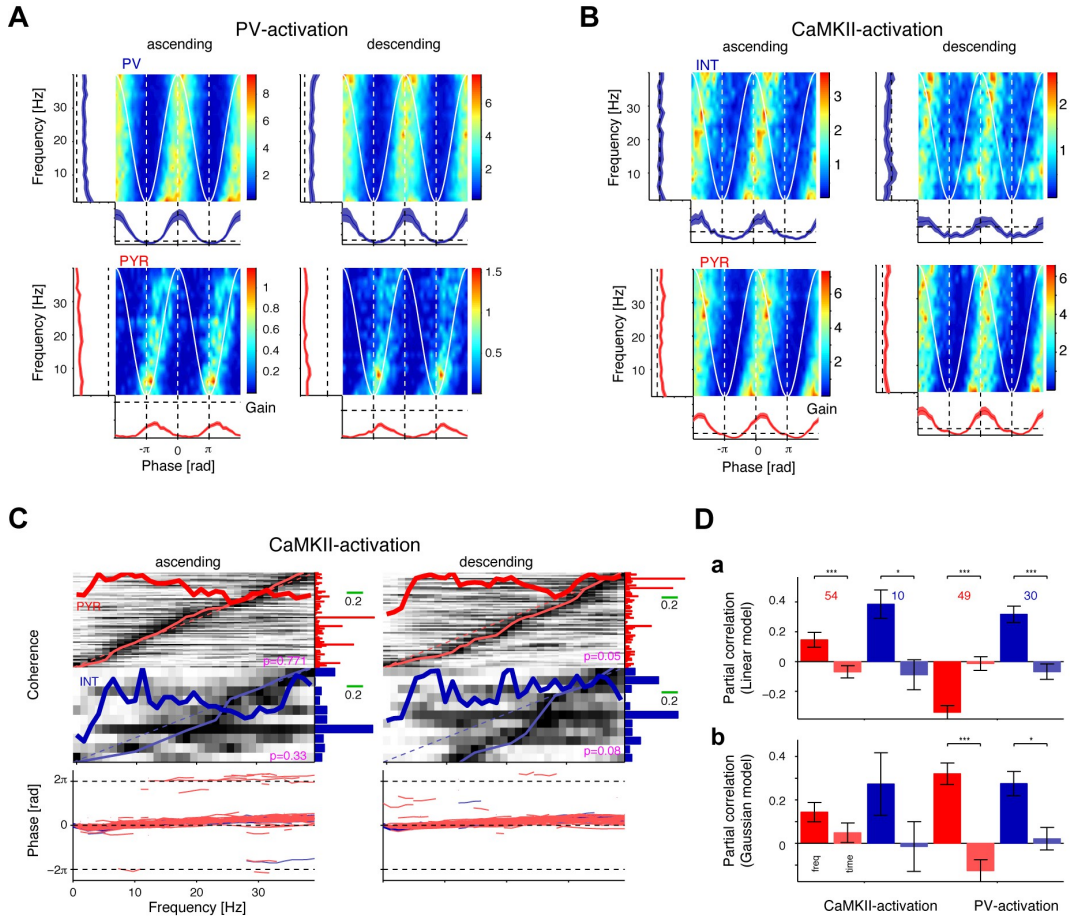

Figure S4. Inhibition-induced theta resonance occurs regardless of chirp direction

(**A**) Spiking gain maps during PV activation, resolved by chirp-pattern direction, frequency, and phase (conventions are identical to **Figure 3A**). (**B**) Same as **A**, during CaMKII activation. Chirp direction influences frequency-dependent marginal gain, especially in directly-activated cells (see frequency marginals for PV in **A** and PYR in **B**). Yet regardless of chirp direction, PYR spike at theta-band chirp troughs specifically during PV activation. (**C**) Coherence and phase plots for light-activated units during ascending (left) and descending (right) chirp-pattern application in CaMKII animals (complements **Figure 4D**, conventions are identical). Regardless of chirp direction, individual light-modulated cells spike at narrow frequency bands, with preferred frequencies distributed over the entire chirp range (0-40 Hz; p>0.05, Kolmogorov-Smirnov test). (**D**) Chirp frequency predicts coherence consistently better than time. **a**, Linear model. Frequency partial correlation (partial correlation between spiking coherence and chirp frequency, taking into account the linear effect of time in chirp) and time partial-correlation (between coherence and time, taking into account the linear effect of frequency) are shown (mean±SEM). **b**, Gaussian model. Coherence was fitted with 1D unimodal Gaussians, separately in the frequency (frequency model) and time (time model) domains, and each model was used to predict the coherence during ascending and descending chirps. Frequency partial correlation (freq), the correlation between the observed coherence and the coherence predicted from the frequency model, taking into account the (linear) effect of the (non-linear) time model. Time partial-correlation (time), same, with the roles of frequency and time switched. Regardless of the method (linear models, non-linear models; rank correlation approach, **Figure 4E**), frequency is a better correlate of coherence than time during chirp.

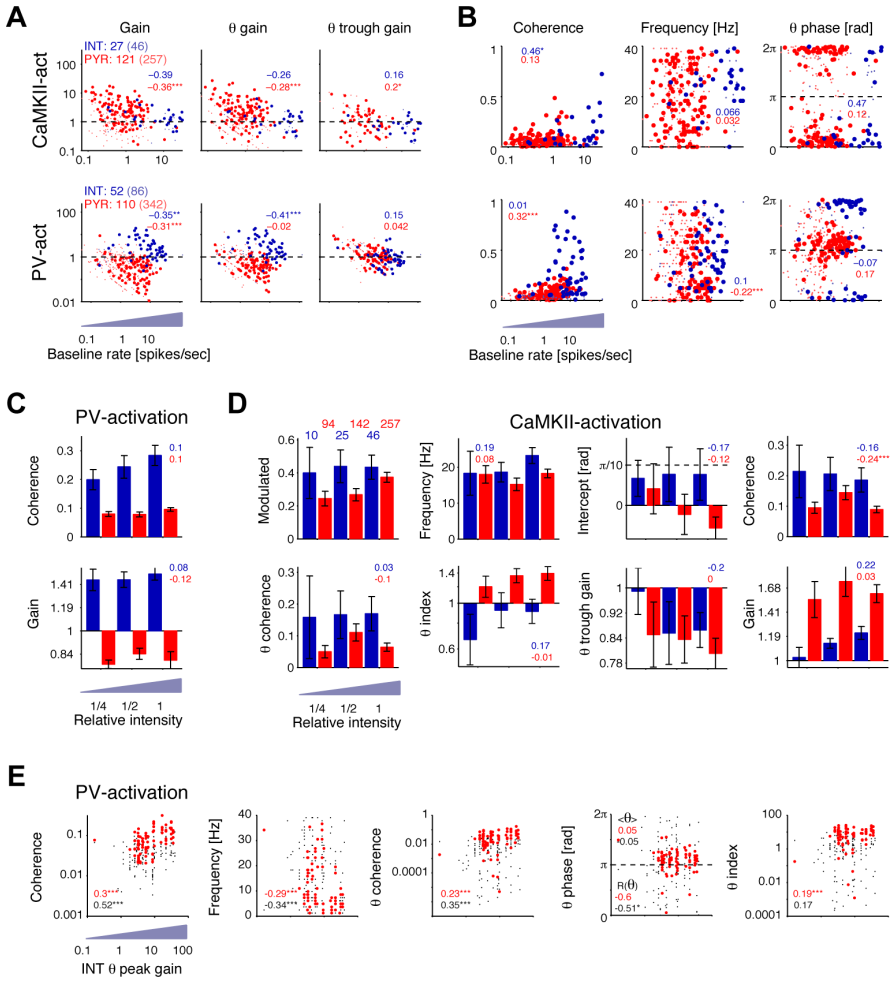

Figure S5. Inhibition-induced PYR spiking depends on inhibitory drive

(**A**) Effect of baseline rate on spiking gain during chirp-pattern application in CaMKII (top) and PV (bottom) animals. Large dots, frequency modulated units; small light dots, units not significantly modulated by the chirp. For each parameter, the rank correlation (modulated units) with the baseline spiking rate is shown in blue/red for INT/PYR; */**/***: p<0.05/0.01/0.005, permutation test. For directly-activated cells (PYR during CaMKII- and PV during PV-activation) spiking gain and theta-band gain are negatively correlated with baseline spiking rate. Theta-trough gain of PYR during PV activation is not significantly correlated with baseline rate. (**B**) During PV activation, PYR coherence and peak frequency depend on baseline firing rate. Data and presentation are identical to **A**. (**C**) Spiking properties of PYR and PV during increasing intensities of PV activation (complements **Figure 5B**). (**D**) Spiking properties during increasing intensities of CaMKII activation. Conventions are identical to **Figure 5B**. PYR coherence depends on intensity (top right; p=0.002, Kruskal-Wallis test) but theta-band preference does not. (**E**) PV theta peak gain predicts PYR spiking during chirp-pattern PV activation. Red dots, light-modulated PYR (n=88); black dots, all PYR recorded simultaneously with a same-shank INT (n=272). The local inhibitory drive, local in space and frequency, was approximated by the INT theta-peak gain. PYR maximal coherence, peak frequency, theta-band coherence, theta-phase variance, and theta index all depend on the local inhibitory drive.

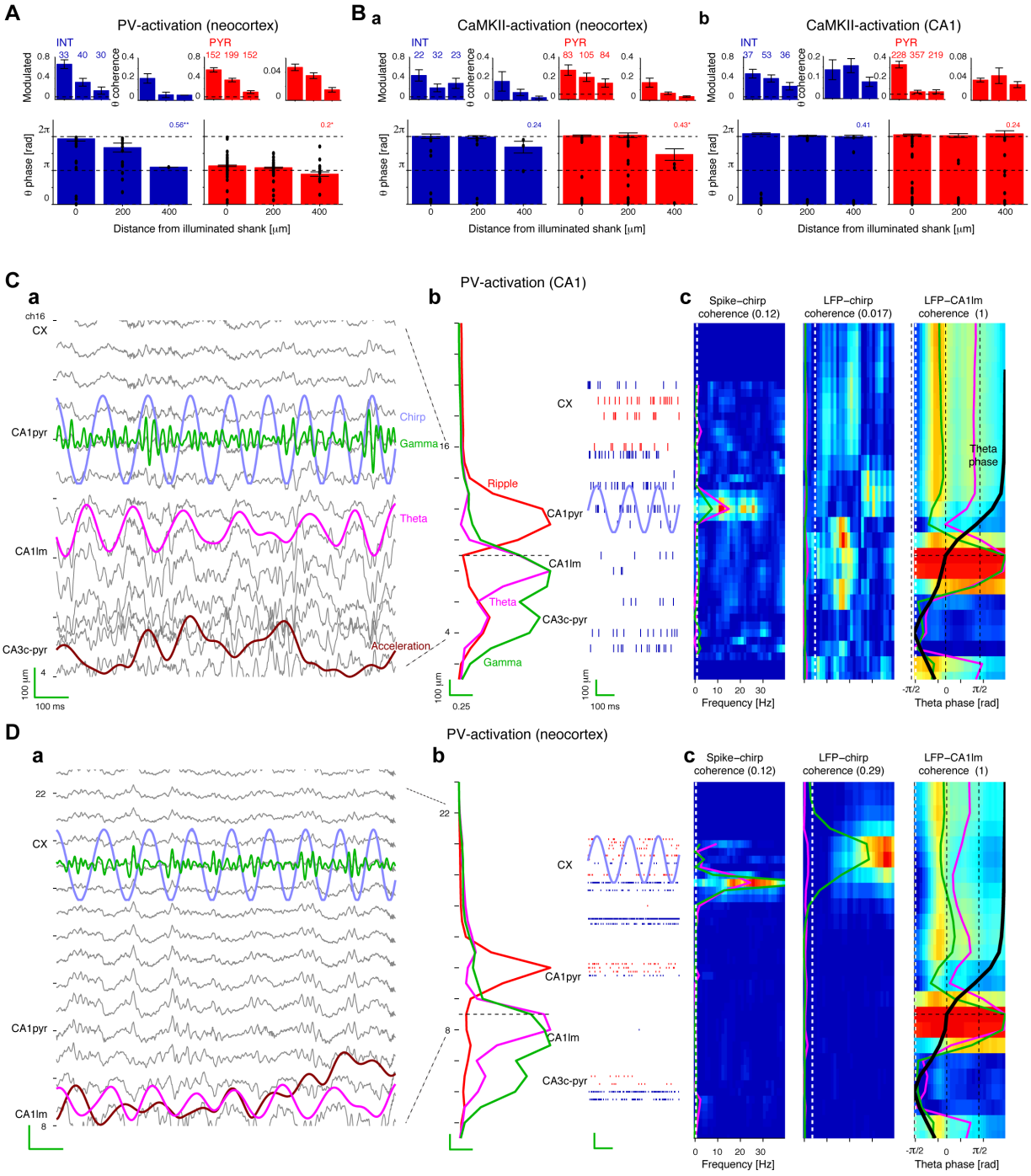

Figure S6. Indirectly activated cells spike at inhibition troughs

(**A**) During chirp-pattern PV activation in neocortex, PV recorded on the illuminated shank spike at theta peak whereas non-local INT spike progressively closer to the trough with increased distance between the light source and the unit. PYR spike at theta trough. Circular-linear correlation coefficients are shown; */**: p<0.05/0.01, χ^2 test. (**B**) In contrast, during chirp-pattern CaMKII activation, theta spiking phase does not depend on distance from the illuminated shank. An exception is some non-local neocortical PYR, which spike on the trough (black dots, individual cells), possibly due to indirect activation of local INT (CaMKII chirp application → local PYR activated directly, in phase → local INT activated indirectly, in phase → distant PYR rebound, anti-phase). (**C,D**) Local PV activation entrains local gamma- but not theta-band rhythms. (**C**) Local chirp-pattern PV activation in CA1 does not modify ongoing theta oscillations. Linear probe (100 μm spacing) recording from the neocortical-

hippocampal axis. The probe was equipped with two fibers, tips terminating about 50 μm above channels 13 and 20. The chirp pattern was applied locally in CA1 (405 nm light intensity, ~2.3 mW/mm^2) during spontaneous exploratory behavior; this resulted in phase-locked spiking of local units but not of distant units or LFP. **a**. One sec snapshot during chirp pattern stimulation. **b**. Depth profile of theta- (4-11 Hz), gamma- (30-80 Hz), and ripple-band (80-250 Hz) power, and theta phase (relative to the channel 9 theta). Right panel, spiking activity during theta-band chirp stimulation. CA1 pyramidal layer corresponds to channel 12. The chirp pattern drives PV spiking in CA1pyr but not in neocortex or deep hippocampus. **c**. Coherence between the chirp pattern and spikes (left) or LFP (right). Purple/green lines show mean theta-band and gamma-band coherence, respectively. White dashed lines show chance coherence (horizontal coherence scale, 0-0.1; coherence color scale, 0-0.12 for spikes and 0-0.017 for LFP). The coherence between chirp and theta-band LFP is not significant. (**D**) Local PV activation in neocortex does not modify local LFP theta. The probe was left in the same position as in **C** (recording 48 hours later). **a**, Chirp-pattern PV activation by a fiber just above channel 20 (approximate 405 nm light intensity on channel 18, 1.7 mW/mm^2). **b**. Spiking in neocortex but not in hippocampus is modulated by the theta-band chirp pattern (PV, in-phase; PYR, anti-phase). **c**. Coherence between the chirp and neocortical spiking is at theta-band and wide-band for PYR and INT, respectively. At higher chirp frequencies, LFP is entrained at gamma frequencies (Cardin et al., 2009), with peak LFP-chirp coherence around 35 Hz and leakage to lower frequencies. Theta is not entrained.

In previous studies (Cardin et al., 2009; Sohal et al., 2009), optogenetic stimulation of regular spiking pyramidal neurons (CaMKII) in the somatosensory cortex of anesthetized mice resulted in reliable unit driving at low frequencies but progressively decreasing responses at higher frequencies (Cardin et al., 2009). Although a similar trend was observed here (**Figure S3Ba** bottom, orange curve), the previous study differed from ours in several aspects. First, in previous work the mice were anesthetized. Second, pulses instead of sinusoid chirp patterns were used. Third, the applied blue light was about 50 times stronger than in our experiments, and therefore a much larger circuit was involved. In those studies, photostimulation of neocortical PV interneurons resulted in entrainment of spikes of fast spiking neurons and phase locking of local gamma oscillations up to 40 Hz (Cardin et al., 2009; Sohal et al. 2009), similar to the current observations (**Figure S6D**).

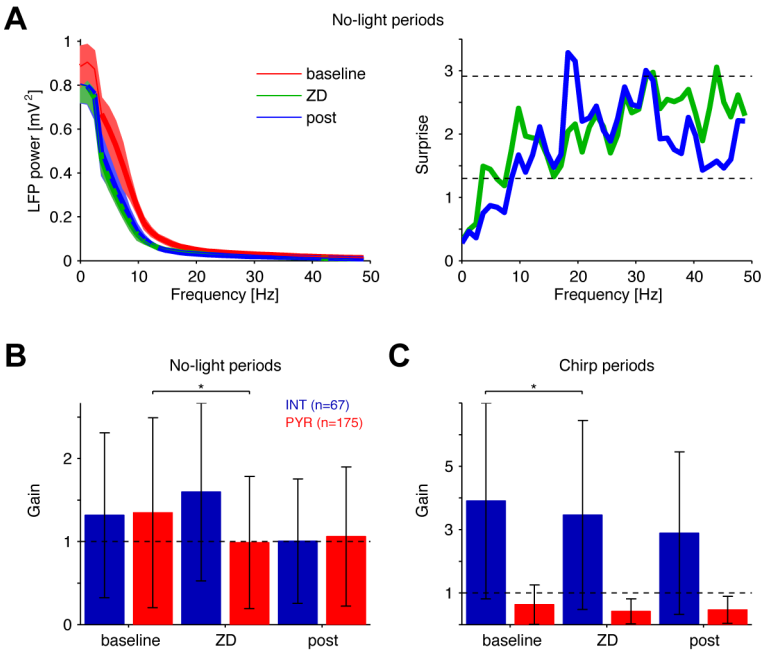

Figure S7. Global effects of ZD7288 on extra cellular field and spiking activity

(**A**) Effect on LFP. **Left**: Power spectrum (0-50 Hz) of the LFP during and after ZD7288 injection to CA1 radiatum/lacunosum-moleculare (consecutive duration matched periods, chirp periods excluded; 102±13 sec per period per animal; n=5 PV::ChR2 mice). Spectral power is reduced during and after ZD injection (green and blue curves; mean±SEM) relative to baseline. **Right**: consistent with this, surprise values are high; significance is indicated by the upper dashed line (Bonferroni-corrected paired t-test; p=0.05). (**B**) Effect on spontaneous spiking. Spiking gain (median±MAD) of interneurons and PYR before, during, and after ZD injection is shown. Epochs are the same as in **A**. Following ZD injection, PYR (but not INT) spiking is slightly diminished (p=0.011, Wilcoxon's paired signed-rank test; p>0.05 for all other comparisons). All 67/175 INT/PYR recorded from n=5 mice are included. (**C**) Effect on frequency-independent spiking during chirp-pattern PV activation. During ZD injection, INT gain is slightly reduced relative to baseline (p=0.03; p>0.05 for all other comparisons). INT are activated and PYR are silenced by the chirp during all 3 epochs.

SUPPLEMENTAL EXPERIMENTAL PROCEDURES

Animal procedures

For the expression of ChR2 in PYR cells, we injected adeno-associated virus (rAAV5/CaMKIIa-hChR2(h134R)-EYFP; CaMKIIa, calcium/calmodulin-dependent protein kinase II alpha promoter; EYFP, enhanced yellow-fluorescent protein) produced by the University of North Carolina viral core (viral titer estimated at $4x10^{12}$ IU/ml; courtesy of Dr. Karl Deisseroth) into two-month old wild-type mice (n=2). A single 0.2 mm diameter craniotomy was made at PA -1.6/ML 1.1 mm and small amounts of viral solutions (55 nl) were injected at 5 depths (CX: DV 0.7±0.2 mm; CA1: DV 1.1±0.2 mm) using a volume-based micro-injector (Nanoject II, Drummond) mounted on a stereotactic frame (Kopf Inc.). Following the injections, the scalp was sutured and animals allowed to recover for at least 2 weeks before implantation. We also cross-bred male mice heterozygous for a loxP-ChR2 conditional allele (Rosa-CAG-LSL-ChR2(h134R)-EYFP-WPRE; Ai-32, Allen Institute; Madisen et al., 2012) with homozygous females expressing Cre recombinase under the control of the CaMKII promoter (B6.Cg-Tg(Camk2a-cre)T29-1Stl/J, Jackson Labs). At the age of 8 weeks pups were genotyped and positive animals were used for implantation (n=2 mice). For the expression of ChR2 in PV interneurons, we cross-bred male Ai-32 mice with homozygous females expressing Cre recombinase under the control of the PV promoter (and B6;129P2-Pvalb tm1(cre)Arbr/J, Jackson Labs). 8 such mice were used for chronic implantation and 5 for acute experiments.

Animals were implanted with multi-shank diode-probes following previously-described procedures (Stark et al., 2012). Briefly, diode-probes were constructed by coupling blue LEDs (470 nm; LB P4SG, Osram; 2 mm diameter) and/or violet laser-diodes (LD; 405 nm; KES-410ACA, Sony; 5.6 mm diameter, clipped to 4.1 mm) to optical fibers (AFS50/125, Thorlabs) etched to a point. Each diode-fiber assembly was attached to a shank of commercially-available silicon probes (32-site/4-shank probes, Buzsaki32SP; 64-site/6-shank probes, Buzsaki64SP; or 32-site/1-shank probes, A1-32 edge; NeuroNexus). Diodes were driven by a 16-channel custom-made precision current source (LEDs: 1-60 mA; LDs: 26-36 mA). At the time of implantation, the light output at the tip of the shanks was 35±7 µW (mean±SD; n=48 470 nm LEDs) or 231±62 µW (n=6 405 nm LDs). Fiber tips were located ~50 µm above the top recording site; this configuration yielded maximal blue light intensity of approximately 1.5 mW/mm^2 at the shank center (Stark et al., 2012). Mice were tethered by one ultralight cable for multi-channel neuronal recordings and a second cable for multi-channel optical stimulation.

Recording and stimulation procedures

Probes were implanted at the injection site (virus injected mice) or at PA -1.6/ML 1.1 mm (transgenic animals). During the surgery, the probes were lowered to a depth of 0.4-0.7 mm. After allowing the animals to recover for at least 48 hours, recordings were initiated. Neural activity was filtered (1-5000 Hz), amplified (20x by Plexon headstages and 50x by an RC Electronics system), and digitized (16 bit, 20 kHz) on a 128-channel DataMax recording system (RC Electronics). Head acceleration was measured by a 3-axis accelerometer (ADXL-330, Analog Devices) integrated into the diode-driving cable and recorded continuously by the DataMax system. Recordings and photostimulation were carried out in the home cage during spontaneous behavior. Signals were generated by custom code written in MATLAB (MathWorks) and converted by digital signal processors (RX5 and/or RX6, TDT) into analogue

signals controlling the current source output. Applied currents were recorded by the DataMax system.

At each location in the brain, neuronal activity was inspected for spontaneous spiking activity, and if encountered, a baseline period of at least 15 minutes was recorded followed by photostimulation. After each session the probe was either left in place or moved (35-70 μm steps), and the brain was allowed to settle overnight. The linear ascending (or descending) chirp had a waveform (**Figure 2**) defined by $x(t)=\cos(\pi+2\pi f_0 t+\pi(f_1-f_0)t^2/T)$ with parameters f_0=0 (or 40) Hz, f_1=40 (or 0) Hz, T=10 sec, Δt=1/6000 sec. For LEDs (which exhibited linearly-increasing light output at increasing currents), the actual current was $I(t)=I_{max}(x(t)+1)/2$, whereas for LDs (which exhibit linear output only in a narrow range above I_{TH}) the applied current was $I(t)=I_{TH}+(I_{max}-I_{TH})(x(t)+1)/2$. I_{max} was set manually to be the lowest current that evoked consistent spiking of one or more cells recorded simultaneously on the illuminated shank during 50 ms light pulses; most units were also tested with higher and lower intensities (**Figure 5**). "White noise" (**Figure 4**) x(t) was generated by convolving uncorrelated zero-mean white-noise r(t) with an exponential ($t\cdot\exp(-t/\tau)$; τ=3 ms; Δt=1/6000 sec). The same 1-sec long pattern was used in all experiments. The actual current output varied and was $I(t)=\mu+x(t)\sigma$, where (μ,σ) were typically set to ($2I_{max}/3$, $I_{max}/9$) for LEDs and to ($I_{TH}+2(I_{max}-I_{TH})/3$, $(I_{max}-I_{TH})/9$) for LDs, keeping I_{max} within the 3 SD range and excluding non-positive (or sub-I_{TH}) values.

I_h blocking experiments

PV::ChR2 mice (n=5) were anesthetized (urethane, 1.5 gr/kg) and placed in a stereotactic device. Ground and reference screws were inserted above the cerebellum, and two craniotomies were made: 1.4 by 0.2 mm, centered at ML/PA 1.1/1.6 mm oriented 45° to the midline (long axis of the right hippocampus); and 0.2 mm diameter at ML/PA 1.9/1.14 mm. After the dura mater was excised from the elongated craniotomy, a pipette (tip size diameter 30-50 μm) back-filled with an I_h blocker (ZD7288, Tocris; 0.1-1M) held by a Nanoject II (Drummond) was oriented at an angle of 30° to the inter-aural line and 30° to the vertical and inserted via the smaller craniotomy to the CA1 radiatum/lacunosum-moleculare (depth of 1500-1700 μm and retracted 100 μm). A six-shank diode-probe (Buzsaki64sp; 10 recording sites/shank, 20/200 μm spacing between sites/shanks) equipped with six 470 nm LEDs was inserted via the elongated craniotomy to the neocortex, and both craniotomies were covered with mineral oil. Body temperature was kept at 37° using two water-base heating pads. The probe was lowered in 150 μm steps followed by 5-minute pauses. CA1 pyramidal layer was recognized by the sudden appearance of ripples and spontaneous spiking 200-500 μm after neocortical spiking was diminished. Following a period of baseline recording, a continuous train of regularly spaced 10 sec linear chirps was applied to each shank. After 2-10 chirps were applied to each shank, 200 nl of the drug were injected over 6 minutes, during which 2-6 chirps were applied to each shank. Subsequently at least 10 more chirps/shank were applied.

Histology

Mice were anesthetized with pentobarbital injection, perfused with saline and 4% paraformaldehyde before their brains were rapidly removed. Coronal sections (80 μm) were cut on a vibratom (Leica, VT1000S) and collected in PBS. After 2 washes in PBS (10 min each), sections were permeabilized in PBS containing 0.2% gelatin and 0.2% Triton-X100 (PBS*) for 1 hour and processed for immunostaining by overnight incubation at 4°C with

polyclonal rabbit antibodies anti-PV (1:1000; PV 25, Swant) diluted in PBS*. After 2 washes (30 minutes each) in PBS, sections were incubated for 2 hours at room temperature with secondary antibodies (goat anti-rabbit IgGs conjugated to Alexa Fluor 555 dyes; 1:3000; Molecular Probes). After 3 washes (20 minutes each), sections were mounted in Fluoromount (Sigma) and imaged with a confocal laser-scanning microscope equipped with a 63x objective.

Cell type classification

Offline, spikes were extracted from the wide-band (1-5000 Hz) signals, the waveforms were projected onto a common basis obtained by principal component analysis (PCA) of the data, and sorted into single units automatically (Harris et al. 2000) followed by manual adjustment. Units were required to fulfill the following criteria: (1) amplitude: peak-to-peak amplitude above 50 μV; (2) morphological isolation: L-ratio (Schmitzer-Torbert et al. 2005) below 0.05; (3) temporal isolation: inter-spike-interval histogram with a clear refractory period (count in the first 2 ms below 0.2 of the expected count given the counts in the first 20 ms; Fee et al. 1996). A total of 324 neocortical (chronic recordings) and 1331 (1089 chronic, 242 acute) CA1-pyramidal layer units conformed to these criteria (**Figure S1C**).

Units were classified as putative excitatory cells (PYR) or inhibitory interneurons (INT) based on short-latency features in cross-correlation histograms in the absence of light stimulation (Barthó et al. 2004), responses to 50 ms light pulses, and/or waveform features. Units that participated as a trigger in a cross-correlation histogram that exhibited a significant ($p<0.001$, convolution method; Stark and Abeles, 2009) peak in the mono-synaptic time range (-5 to 5 ms) were assumed to be excitatory cells (i.e. PYR), whereas units that exhibited a significant trough were assumed to be inhibitory cells (INT) (**Figure 1B**, **Figure S1A**). Of 22,341 CCHs (1413 units from chronic recordings), 1291 (5.8%) exhibited significant features (1209/82 peaks/troughs), and on this basis 641 (45%) units were tagged as excitatory (615 units) or inhibitory (26 units). In PV animals, units that exhibited a significant ($p<0.001$, Poisson test) increase in spiking rate during 50-70 ms DC pulses given on the local shank were tagged as PV cells; 93/1041 (9%) units conformed to this criterion. Half of the inhibitory cells (INT) were PV cells (13/26) and no PV cells were excitatory. Thus 615 units were tagged as excitatory and 106 as inhibitory and/or PV light-activated. The remaining half of the units (692/1413, 51%) was not tagged by either method and classified on the basis of waveform shape. For each unit, the single recording site with the maximal peak-to-peak amplitude mean waveform was selected and two waveform features were computed (from the wide-band (1-5000 Hz) traces, digitized at 20 kHz for 32 samples): the trough-to-peak (TP) and the spike width (W; the inverse peak frequency of the spike spectrum, estimated by 1024-point FFT of the zero-padded waveforms). This generated two clearly separable clusters in both brain regions (**Figure S1A**). For objective classification of non-tagged units, a Gaussian mixture model (GMM) was fit to the tagged data obtained by optical stimulation and mono-synaptic connectivity (**Figure S1B**). The cluster centers were (mean±SEM): narrow waveforms (putative INT): TP: 328±9 μs, W: 900±6 μs; wide waveforms (putative PYR): TP: 649±2 μs, W: 1078±5 μs. Thus, units with narrow waveforms and prominent after-spike hyperpolarization were classified as INT, whereas units with wide waveforms and weak after-spike hyperpolarization as PYR (Sirota et al., 2008). The use of the GMM enabled assigning p-value to the classification of each unit, and units with low classification confidence ($p>0.05$) were discarded (22/1413 units, 1.6%). These methods (mono-synaptic connectivity, optical tagging, and spike

waveform features) separated PYR from INT better than single-cell temporal firing statistics (firing rate, auto-correlation histograms), which were used for subjective validation.

Data analysis

For each unit recorded during linear chirp stimulation, the cross-spectral density between the raw spike train and the applied current pattern (both digitized at 1250 Hz) was estimated using multi-taper spectral methods (6 discrete prolate spheroidal sequences, FFT of 1024 points, 50% overlap between adjacent windows; i.e., spectral resolution of 1.22 Hz). We used the raw spike train rather than convolving with a kernel since when firing rates are high as often observed for INT, convolution modifies the spectral estimate in the high frequency range. Coherence and phase estimates were derived from the cross-spectral density. A significance level α (0.05 throughout) was defined, Bonferroni-corrected for the multiple comparisons in the spectral region of interest (ROI, 0-40 Hz), and converted to a multiplier by the inverse normal distribution. Chance coherence (see below) was estimated and multiplied by this factor; higher coherence values in the spectral ROI were deemed significant at the α level. We further required a continuous 5-Hz band of significant coherence; this made the test conservative, but only slightly since the coherence at adjacent frequency bands are correlated due to tapering (auto-correlation full-width at half-height, 4 bins, i.e. 4.88 Hz).

Chance coherence was determined by 4 different methods: (1) permutation test – coherence was computed between the chirp pattern and spike trains selected at random from periods without light stimulation; (2) time reversal – coherence between time-reversed chirp and the original spike train; (3) jittering test – coherence between the chirp pattern and spike trains jittered within a 1 sec time window; (4) high frequency coherence test – the mean coherence in the high frequency range (250-625 Hz). Randomization tests were repeated 1000 times. The objectivity and sensitivity of these procedures were validated using Monte-Carlo spike train simulations, either uncorrelated with the input pattern or tuned to specific phases and/or frequencies. The different methods gave nearly identical results; the permutation (segment randomization) test was the most conservative and used for all analyses.

Since the chirp pattern was not precisely flat at the band of interest, we also computed a “corrected” coherence estimate in which the ROI coherence was divided on a bin-by-bin basis by the normalized chirp spectrum; to account for differences in firing rates, we computed a “scaled” coherence estimate in which the ROI coherence was divided by the square root of the single-unit firing rate (**Figure S2C**). The results reported in the text were not sensitive to these corrections, to the digitization rate, or to multi-taper parameter values.

In a complementary time-domain analysis, we partitioned the chirp pattern into discrete 0.5 sec segments, each of a distinct central frequency (2±1 Hz, 4±1 Hz...). Spikes (of each unit separately) that occurred during this segment were each assigned a frequency and a phase (bin size, $\pi/10$) and the counts in each bin were converted to firing rates. The resulting frequency-phase firing-rate maps were converted to gain maps (divided by the mean firing rate of the same unit in the lack of any light stimulation). For visualization purposes only, maps were averaged over units, linearly interpolated, and color-coded. For an equivalent analysis during WN stimulation and spontaneous LFP, filter banks (zero lag, linear phase FIR) were applied.

Biophysical modeling

To generate spiking regime theta-band resonance we used a minimal circuit biophysical (conductance-based) model of the Hodgkin-Huxley type. The circuit consisted of a PYR, an INT, and possibly an oriens-lacunosum moleculare (OLM) cell, synaptically connected through AMPA excitation and $GABA_A$ inhibition (**Figure 8**). All cells included transient sodium and delayed rectifier currents to describe spiking dynamics. The PYR was modeled using a reduced Traub-Miles neuron (Olufsen et al., 2003) modified to include an h-current (Zemankovics et al., 2010). The INT was modeled using a Wang-Buzsaki (1996) interneuron. The OLM was modeled as in Tort et al. (2007) using a reduction of the multi-compartmental model proposed in Saraga et al. (2003), and included I_h and I_A. Synaptic connections were modeled as in Ermentrout and Kopell (1998); synaptic dynamics had characteristic rise and decay times that depended on the synaptic type (rise times typically fast, decay times slower): the decay time for AMPA excitation was faster than the decay time of $GABA_A$ inhibition, and the $GABA_A$ decay time for INT-generated inhibition was faster than for OLM-inhibition (Rotstein et al., 2005). Synaptic depression was added to the inhibitory synapses using the model proposed by Manor and Nadim (2001).

SUPPLEMENTAL REFERENCES

Ermentrout GB, Kopell N. (1998). Fine structure of neural spiking and synchronization in the presence of conduction delays. Proc. Natl. Acad. Sci. USA 95, 1259-1264

Manor Y, Nadim F. (2001). Synaptic depression mediates bistability in neuronal networks with recurrent inhibitory connectivity. J Neurosci. 21, 9460-9470.

Olufsen MS, Whittington MA, Camperi M, Kopell N. (2003). New roles for the gamma rhythm: population tuning and preprocessing for the Beta rhythm. J. Comput. Neurosci. 14, 33-54.

Saraga F, Wu CP, Zhang L, Skinner FK. (2003). Active dendrites and spike propagation in multi-compartment models of oriens-lacunosum/moleculare hippocampal interneurons. J. Physiol. 552, 673-689.

Tort AB, Rotstein HG, Dugladze T, Gloveli T, Kopell NJ. (2007) On the formation of gamma-coherent cell assemblies by oriens lacunosum-moleculare interneurons in the hippocampus. Proc. Natl. Acad. Sci. USA. 104, 13490-13495.

Wang XJ, Buzsáki G. (1996). Gamma oscillation by synaptic inhibition in a hippocampal interneuronal network model. J. Neurosci. 16, 6402-6413.